









RESEARCH ARTICLE | OCTOBER 18 2023

# Uniformly dispersing and anchoring graphene on GaN nanowire substrate: Application to electrochemical detection of glucose in sweat

Shunji Chen ; Jun Yu ; Jianwei Zhang  ; Hui Huang  ; Hongqian Xiao; Yanjie Tang ; Vladimir G. Dubrovskii ; Haibin Liu; Peiling Xia; Zhefu Chen



*Appl. Phys. Lett.* 123, 163702 (2023)

<https://doi.org/10.1063/5.0172130>



View  
Online



Export  
Citation

CrossMark

# Uniformly dispersing and anchoring graphene on GaN nanowire substrate: Application to electrochemical detection of glucose in sweat

Cite as: Appl. Phys. Lett. **123**, 163702 (2023); doi: 10.1063/5.0172130

Submitted: 13 August 2023 · Accepted: 7 October 2023 ·

Published Online: 18 October 2023



View Online



Export Citation



CrossMark

Shunji Chen,<sup>1</sup> Jun Yu,<sup>2,a)</sup> Jianwei Zhang,<sup>1,a)</sup> Hui Huang,<sup>1,a)</sup> Hongqian Xiao,<sup>2</sup> Yanjie Tang,<sup>2</sup> Vladimir C. Dubrovskii,<sup>3</sup> Haibin Liu,<sup>4</sup> Peiling Xia,<sup>4</sup> and Zhefu Chen<sup>4</sup>

## AFFILIATIONS

<sup>1</sup>Key Laboratory of Integrated Circuit and Biomedical Electronic System, School of Artificial Intelligence, Faculty of Electronic Information and Electrical Engineering, Dalian University of Technology, Dalian 116024, China

<sup>2</sup>Key Laboratory of Liaoning for Integrated Circuits and Medical Electronic Systems, School of Biomedical Engineering, Dalian University of Technology, Dalian 116024, China

<sup>3</sup>Faculty of Physics, St. Petersburg State University, Universitetskaya Embankment 13B, 199034 St. Petersburg, Russia

<sup>4</sup>The School of Kinesiology and Health Promotion, Dalian University of Technology, Dalian 116024, China

<sup>a)</sup>Authors to whom correspondence should be addressed: junyu@dlut.edu.cn; jwzhang@dlut.edu.cn; and huihuang@dlut.edu.cn. Tel.: +86-411-84708096

## ABSTRACT

For deposition of two-dimensional materials (e.g., graphene) on a substrate, self-aggregation and poor anchor strength are still issues. Herein, the GaN nanowire (NW) substrate was employed for electrochemical deposition of reduced graphene oxide (rGO) with satisfying dispersion uniformity and anchor strength. The deposited rGO exhibited flake morphology without agglomeration. Moreover, PtAu and rGO can be simultaneously and uniformly deposited on the GaN NW substrate to realize a PtAu-rGO/GaN electrochemical sensor for glucose detection. In comparison with deposition of PtAu-rGO on a stainless steel (SS) substrate (i.e., PtAu-rGO/SS), PtAu-rGO/GaN demonstrated much higher sensitivity and long-term stability, owing to better dispersion and anchor strength on GaN NW. In addition, with decoration of glucose oxidase (GOx), the GOx/PtAu-rGO/GaN sensor can be used for detecting glucose in human sweat with a low limit of detection of 5  $\mu$ M, a wide linear detection range of 5  $\mu$ M–12 mM, and high long-term stability, which indicates that GOx/PtAu-rGO/GaN sensor is promising for noninvasive glucose detection.

Published under an exclusive license by AIP Publishing. <https://doi.org/10.1063/5.0172130>

As a kind of two-dimensional (2D) materials, reduced graphene oxide (rGO) features high conductivity, carrier mobility, and good mechanical strength,<sup>1</sup> and it is widely used for electrochemical sensor (ECS). However, rGO is normally suffered from agglomeration and mechanical detachment when deposited on substrates,<sup>2–4</sup> which would deteriorate sensing performance.

Meanwhile, detecting glucose in sweat (GIS)<sup>5–9</sup> has aroused increasing attention in recent years, because it can replace the invasive finger prick and be used for real-time monitoring. Currently, commercial portable glucometers are mainly based on enzymatic ECS, but their sensitivity is limited with a limit of detection (LOD) of only  $\sim$ 0.5 mM, which cannot meet the requirement of detecting glucose in human sweat (0.06–1 mM).<sup>6,7</sup>

In order to increasing the sensitivity of enzymatic ECS, electrochemical deposition (ECD) of rGO and noble metals as carrier of

enzyme has been proved to be the one of most effective methods.<sup>2,3,10–13</sup> However, for ECD of rGO, the rGO was deposited by the reduction in GO with an absolute potential larger than 0.9 V ( $<$ –0.9 V), which could inevitably make water electrolyzed and generate hydrogen gas bubbles. When traditional planar substrates (e.g., glass carbon electrode, Au<sup>2–4</sup>) were employed for loading rGO, the electrolysis generated bubbles usually adhered on the substrate and were difficult to leave from the substrate until their sizes became sufficiently large.<sup>14,15</sup> Thus, the ECD of rGO was accompanied by the accumulation and growth of the bubbles, which resulted in the agglomeration of rGO. In addition, rGO was easy to peel from the substrate, due to poor anchor strength of the planar substrate.

Inspired by substrate roughening,<sup>16</sup> vertical nanowire (NW) arrays as a substrate would be useful for trapping 2D materials with good anchor strength. Moreover, substrate roughening can also bring

about good hydrophilicity,<sup>15,17–20</sup> which reduces the contact area between bubble and substrate by forming a wetting film on the substrate. The decrease in contact area will facilitate bubble leaving from the substrate, and it also reduces the size of bubbles on the substrate.<sup>15,17–20</sup> Thus, the NW arrays with the rough surface would be helpful for loading 2D materials with uniform dispersion. Especially, GaN NW has the advantages, such as (1) high thermal conductivity, good electroconductibility, and chemical stability<sup>21</sup> and (2) as a mainstream third-generation semiconductor, GaN material can be mass produced with low cost, and precise control on composition and morphology can also be realized by using mature industrial technologies. Thus, GaN NW would be a promising substrate for loading rGO.

In this paper, the GaN NW array was employed for loading rGO with satisfying dispersion uniformity and anchor strength. Moreover, PtAu and rGO can be simultaneously and uniformly deposited on the GaN NW substrate (PtAu-rGO/GaN) by one-step ECD. Bimetallic PtAu is expected to achieve higher catalytic activity and stability due to the synergistic effect of Pt and Au. The PtAu-rGO/GaN sensor was applied to detect glucose in neutral solution with high sensitivity and good stability. In addition, the presence of PtAu also can enhance the sensitivity of the enzymatic sensor. With decoration of glucose oxidase (GOx), GOx/PtAu-rGO/GaN sensor can be used for detecting glucose in human sweat.

Fabrication process of PtAu-rGO/GaN sample was illustrated in Fig. 1(a), and its SEM image was shown in Fig. 1(b). As shown in upper image of Fig. 1(b), GaN NW array with an average length of 15  $\mu\text{m}$  and a diameter of 80 nm was vertically grown on the GaN-L

coated sapphire substrate, and the NWs can significantly increase the surface roughness of the substrate. The HR-TEM image (Fig. S1) indicates the single-crystalline structure of the GaN NW with a d-spacings of 2.76 and 2.44  $\text{\AA}$ , which coincides with (100) and (011) plane of hexagonal GaN (JCPDS 50-0792), respectively.<sup>21</sup>

After the ECD process, a thin layer of sheet-like PtAu-rGO was anchored on the NW surface [Fig. 1(b)], and the color of the sample was changed from yellow to black (Fig. S2). Abundant holes (formed by electrolysis induced bubbles leaving from the substrate) with the size of  $\sim 10 \mu\text{m}$  are found on the PtAu-rGO layer [Fig. 1(c)], which is beneficial for mass transportation of analytes. The reason for uniform dispersion of rGO on GaN NWs was attributed to the reduced size and easy detachment of electrolysis induced bubbles on the GaN NW substrate (detailed explanation was shown in the supplementary material S5). Magnified SEM image [indicated by black box in Fig. 1(c)] shows that the NWs cross link into a network for loading rGO sheets and a part of NWs puncture through rGO sheets. Because of different puncturing directions of NWs, the rGO sheets can be firmly anchored without detachment. In comparison, the PtAu-rGO deposited on the planar stainless steel (SS) substrate [Figs. 1(d) and 1(e)] and the planar GaN-L/sapphire substrate (Fig. S3) show agglomeration with much larger hole size of  $\sim 50 \mu\text{m}$ . Moreover, detachment is observed from the SEM image [indicated by red arrow in Fig. 1(e)] and optical photograph (Fig. S2), which should result from the poor anchor strength of the SS substrate. Thus, it can be concluded that the NW array plays an important role in dispersing and anchoring rGO.

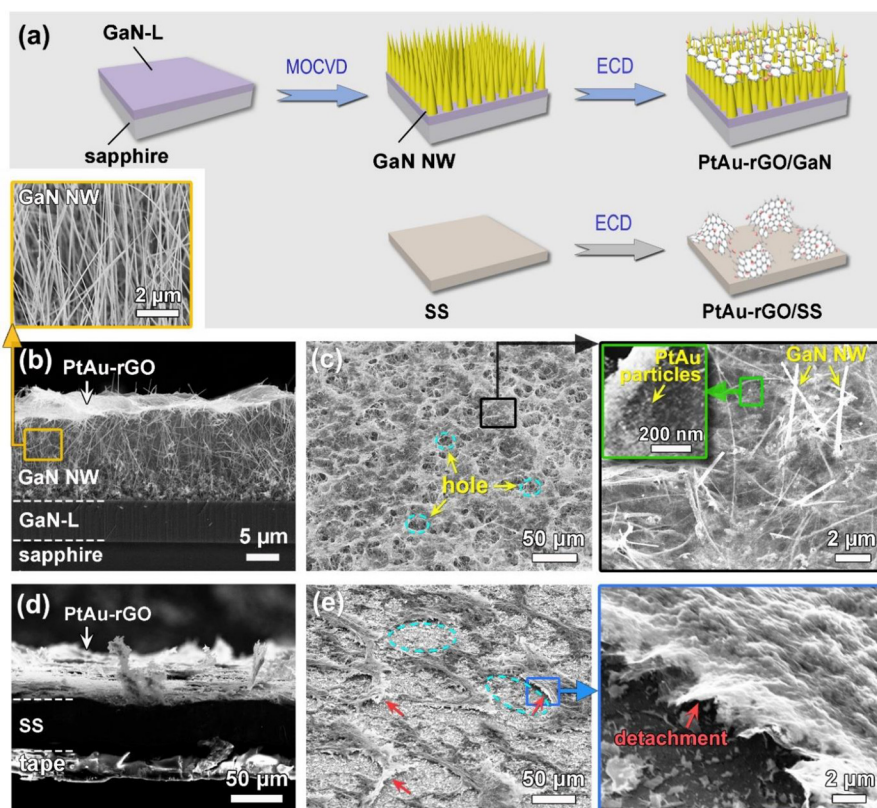


**FIG. 1.** Fabrication process and the corresponding surface morphology of PtAu-rGO/GaN and PtAu-rGO/SS samples. (a) Schematic illustration of the sample fabrication. SEM images (cross-sectional view) of (b) PtAu-rGO/GaN and (d) PtAu-rGO/SS. Magnified SEM images (45° side view) of PtAu-rGO deposited on (c) GaN NW and (e) SS.

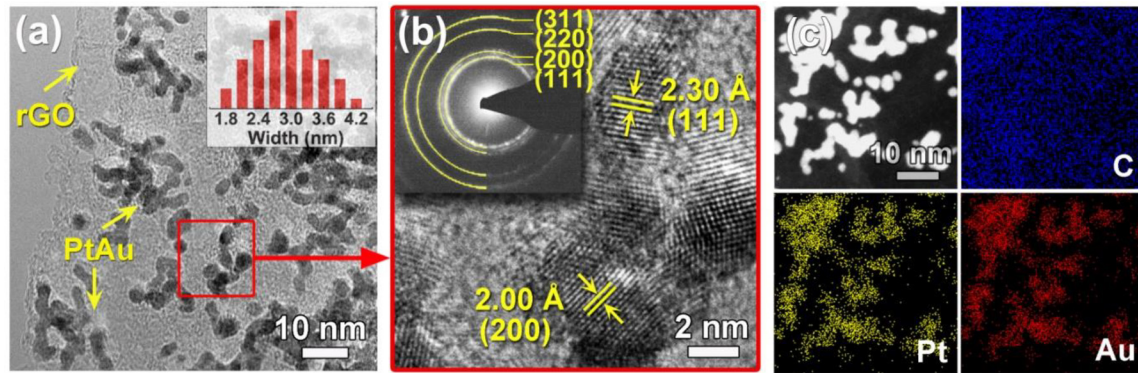


**FIG. 2.** TEM characterizations of PtAu-rGO/GaN. (a) TEM image, (b) HR-TEM image, and (c) HAADF-EDS mapping of PtAu-rGO/GaN. Inset of (a) and (b): the size distribution of PtAu particles and the corresponding SAED pattern.

The inset of Fig. 1(c) (green box) shows that PtAu particles with the size of less than 10 nm are uniformly dispersed on the rGO layer. In comparison, for the PtAu-rGO (WSC)/GaN sample (i.e., ECD without sodium citrate), PtAu particles become aggregated with much larger diameter of  $\sim 370$  nm (Fig. S4). Thus, sodium citrate is important for obtaining small-sized and well-dispersed PtAu particles, because sodium citrate can stabilize and prevent PtAu from aggregation.<sup>22</sup> SEM-EDS mapping analysis of PtAu-rGO/GaN confirms the uniform distribution of Pt and Au elements on rGO, which is anchored by GaN NWs [Fig. S5(a)].

TEM image of PtAu-rGO deposited on GaN NW was shown in Fig. 2(a). The PtAu particles tend to lineup as nanowires with an average width of 3 nm (inset). The measured Pt/Au atomic ratio is 1.16:1

for PtAu-rGO/GaN [Fig. S5(b)], which is close to the molar ratio during preparation. The diffraction rings in selected area electron diffraction (SAED) pattern indicates that these PtAu particles are polycrystalline [inset of Fig. 2(b)]. It has known that the d-spacings is 2.25 Å for the face centered-cubic (fcc) Pt (111) (JCPDS 04-0802) and 2.36 Å for the fcc Au (111) (JCPDS 04-0784), respectively.<sup>23</sup> For the PtAu particles, the d-spacings of 2.30 and 2.00 Å [corresponding to the (111) and (200) planes] are in between that of the fcc Pt and fcc Au. Moreover, HAADF-EDS mapping shows that Pt and Au are uniformly distributed on the particles [Fig. 2(c)]. Thus, the PtAu should be alloy phase, which is consistent with the result of GI-XRD analysis (Fig. S6).

The surface state of PtAu-rGO/GaN was analyzed by XPS. In the Pt 4f spectrum [Fig. 3(a)], the two peaks at 71.3 eV (Pt 4f<sub>7/2</sub>) and

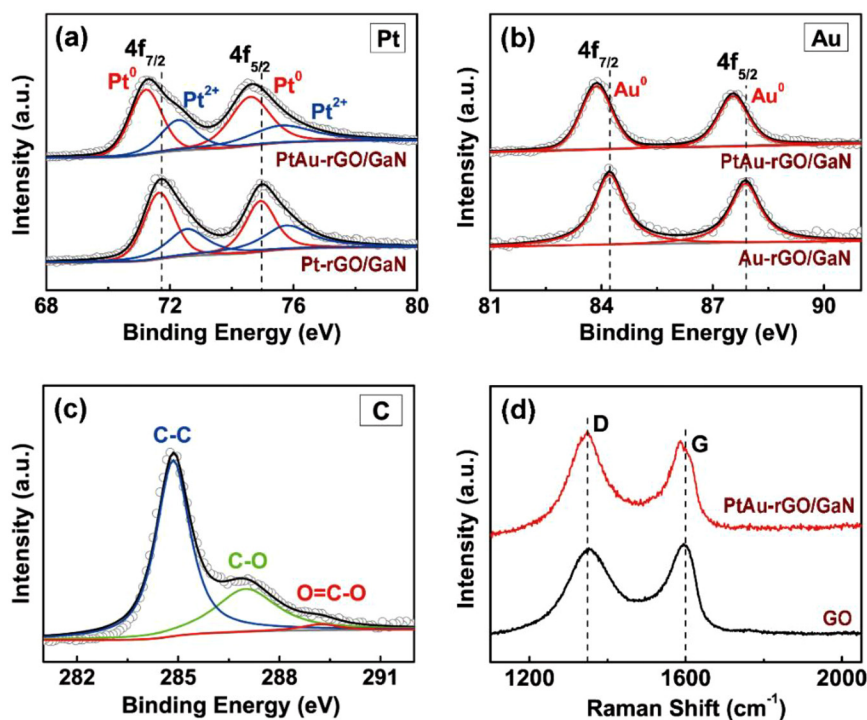


**FIG. 3.** XPS spectra of (a) Pt 4f and (b) Au 4f of the PtAu-rGO/GaN, Pt-rGO/GaN, and Au-rGO/GaN. (c) XPS spectrum of C 1s of PtAu-rGO/GaN. (d) Raman spectra of GO and PtAu-rGO/GaN.



74.6 eV (Pt  $4f_{5/2}$ ) can be assigned to metallic Pt.<sup>24</sup> Another two weak peaks at 72.3 eV (Pt  $4f_{7/2}$ ) and 75.6 eV (Pt  $4f_{5/2}$ ) can be assigned to Pt oxide.<sup>24</sup> In the Au 4f spectrum [Fig. 3(b)], the peaks at 83.8 eV (Au  $4f_{7/2}$ ) and 87.5 eV (Au  $4f_{5/2}$ ) can be assigned to the metallic Au.<sup>24</sup> In comparison with the Pt-rGO/GaN and Au-rGO/GaN, the Pt peaks and Au peaks gradually shift to the lower binding energies in PtAu-rGO/GaN, indicating the electronic changes after the formation of the PtAu alloy.<sup>1,25,26</sup> Figure 3(c) shows the C 1s spectrum of PtAu-rGO/GaN. There are three peaks at 284.84, 287.02, and 289.22 eV corresponding to C-C, C-O, and O=C-O bonds of rGO, respectively. The C-O/C-C peak ratio of PtAu-rGO/GaN is much lower than that of reported GO material, which indicates that GO was reduced into rGO during the ECD step.<sup>2</sup> The rGO can increase the conductivity of PtAu-rGO/GaN.

Raman spectroscopy was carried out to investigate the structural change during the ECD of GO. As shown in Fig. 3(d), GO has two characteristic peaks at  $\sim 1349$  and  $\sim 1594$   $\text{cm}^{-1}$ , which corresponds to the D-band and G-band, respectively.<sup>27</sup> It has been reported that reduction in GO into rGO can make G-band shift to a lower wave number, due to the increase in-plane crystalline of  $\text{sp}^2$ -bond carbon atoms.<sup>2,28</sup> After ECD, the G-band of PtAu-rGO/GaN ( $\sim 1584$   $\text{cm}^{-1}$ )

shows a red-shift compared to that of GO ( $\sim 1594$   $\text{cm}^{-1}$ ), which indicates that the GO has been reduced into rGO. The result agrees with the above-mentioned XPS analysis.

Detecting glucose in 0.1 M PBS electrolyte was carried out by using the PtAu-rGO/GaN as working electrode in CV measurement. As shown in Fig. 4(a), an increase in anodic current can be observed when glucose (10 mM) was added into the electrolyte. In the positive scan, three anodic peaks are observed, i.e., peak-I at  $-0.15$  V can be attributed to the electrochemical adsorption of glucose which forms the related intermediates, peak-II at 0.30 V represents the formation of Pt(Au)-OH species which can oxidize the intermediates on PtAu, and peak-III at 0.6 V represents the formation of PtAu-oxide which can inactivate glucose oxidation.<sup>29-31</sup> In the negative scan, a cathodic peak at  $-0.15$  V can be attributed to the reduction of PtAu-oxide, i.e., re-activate the PtAu for glucose oxidation.<sup>29-31</sup>

Effect of potential scan-rate on CV response of the PtAu-rGO/GaN sample was measured in 0.1 M PBS solution containing 10 mM glucose. As shown in Fig. 4(b), anodic peak current increases linearly with the square root of scan-rate (inset), which indicates that glucose oxidation on PtAu-rGO/GaN is a diffusion-controlled process.<sup>32,33</sup>

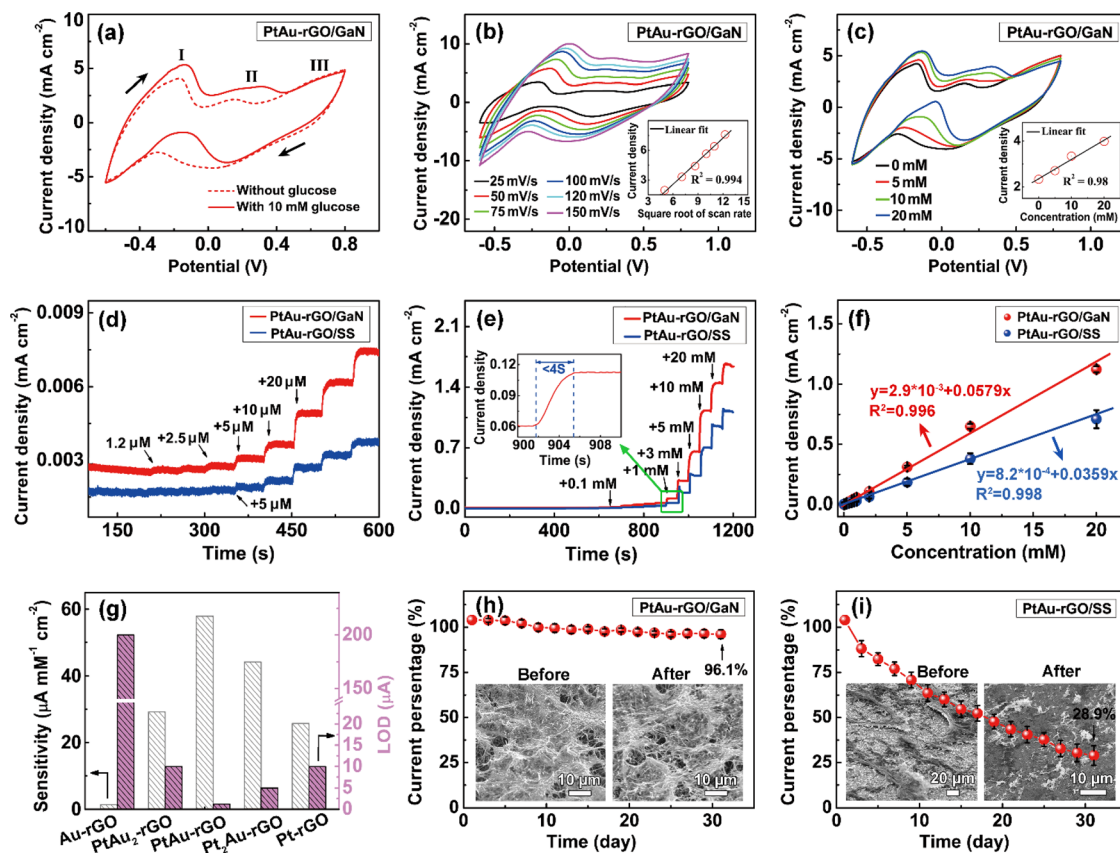


**FIG. 4.** Electrochemical performances of PtAu-rGO/GaN and PtAu-rGO/SS to glucose. (a) CV responses of PtAu-rGO/GaN to 10 mM glucose (scan rate:  $50 \text{ mV s}^{-1}$ ). (b) Effect of scan rate ( $25\text{--}150 \text{ mV s}^{-1}$ ) on CV curve in 10 mM glucose (inset: relationship between the peak current density and scan-rate). (c) Dependence of response current on glucose concentrations (0–20 mM) with a fixed scan rate of  $50 \text{ mV s}^{-1}$ . Amperometric response of PtAu-rGO/GaN and PtAu-rGO/SS with successive addition of glucose at (d) a low concentration range of  $1.2\text{--}80 \mu\text{M}$  and (e) a high concentration range of  $80 \mu\text{M}\text{--}60 \text{ mM}$  (inset: magnified curve at 1 mM). (f) Relationship between response current and glucose concentration. (g) Comparison of sensitivity and LOD of the samples with different Pt/Au ratios. Long-term stability of (h) PtAu-rGO/GaN and (i) PtAu-rGO/SS (inset: SEM images of the samples before and after one-month measurement).

Then, the dependence of response current on glucose concentration was measured with a fixed scan-rate of  $50 \text{ mV s}^{-1}$  [Fig. 4(c)]. It can be seen that the anodic current of peak-II can increase linearly with increasing glucose concentrations (inset).

With an optimal applied potential of  $0.5 \text{ V}$ , the amperometric response of the PtAu-rGO/GaN sample was measured by step increases of glucose concentration from  $1.2 \mu\text{M}$  to  $60 \text{ mM}$  in PBS electrolyte [Figs. 4(d) and 4(e)]. Clearly, an LOD of  $1.2 \mu\text{M}$  [Fig. 4(d)] and a response time less than  $4 \text{ s}$  can be realized [inset of Fig. 4(e)]. Based on the results, the current-concentration relationship is plotted in Fig. 4(f). It can be seen that PtAu-rGO/GaN has a linear detection range of  $1.2 \mu\text{M}$ – $20 \text{ mM}$  ( $R^2 = 0.996$ ) with a sensitivity of  $57.9 \mu\text{A}\cdot\text{mM}^{-1}\cdot\text{cm}^{-2}$ . In contrast, the amperometric response of the PtAu-rGO/SS sample was also measured, and it showed a LOD of  $5 \mu\text{M}$  and a linear detection range of  $1.2 \mu\text{M}$ – $20 \text{ mM}$  ( $R^2 = 0.998$ ) with a sensitivity of  $35.9 \mu\text{A}\cdot\text{mM}^{-1}\cdot\text{cm}^{-2}$  [Figs. 4(d) and 4(f)]. Thus, in comparison with PtAu-rGO/SS, about 4-fold and 1.6-fold improvement in LOD and sensitivity is realized for PtAu-rGO/GaN, respectively. The improved response current in PtAu-rGO/GaN should result from its larger active surface area [Fig. S7(a)] and higher charge-transfer rate [Fig. S7(b)], due to the uniform dispersion and good anchor strength of PtAu-rGO on GaN NW substrate.

Moreover, the influence of the Pt/Au molar ratio on sensing performance was also investigated, and a series of  $\text{Pt}_x\text{Au}_y\text{-rGO/GaN}$  ( $x, y = 0, 1, 2$ ) samples were prepared and measured (Figs. S8–S13). Based on the measured results (Table S1), the relationship between the sensing performance (including LOD and sensitivity) and the Pt/Au molar ratio is plotted in Fig. 4(g). Obviously, the Pt/Au molar ratio of 1/1 (i.e., PtAu-rGO/GaN) is optimum for glucose detection. The improvement on sensing performance can be attributed to the size effects (Fig. S8) and the synergy of Pt and Au (Fig. S10).

Long-term stability is an important parameter for practical application. After one-month measurement of PtAu-rGO/GaN and PtAu-rGO/SS samples to  $2 \text{ mM}$  glucose (the amperometric measurement was carried out once every 2 days), the current retention of PtAu-rGO/GaN is  $96.1\%$  [Fig. 4(h)], which is much higher than that of PtAu-rGO/SS [ $28.9\%$ , Fig. 4(i)]. Surface morphology of two samples after one-month measurement was characterized, and it can be found that PtAu-rGO was partially peeled off from the planar SS substrate [inset of Fig. 4(i)], while it remained steadily anchored on the GaN NW substrate [inset of Fig. 4(h)]. The result confirms that PtAu-rGO/GaN has higher mechanical stability than PtAu-rGO/SS, which leads to the improvement of long-term stability in PtAu-rGO/GaN.

With the decoration of GOx, the GOx/PtAu-rGO/GaN sensor was fabricated and employed for detecting glucose in human sweat [Fig. 5(a)]. Selectivity of the sensor is especially important for glucose detection. In a real sweat sample, the interfering molecules generally contain NaCl, lactic acid (LA), urea, ascorbic acid (AA), uric acid (UA), etc., and the concentration of glucose is more than 10-fold higher than that of interfering molecules.<sup>34,35</sup> Thus, the amperometric response of GOx/PtAu-rGO/GaN sensor was measured with adding  $1 \text{ mM}$  glucose and  $0.1 \text{ mM}$  interfering molecules to  $0.1 \text{ M}$  PBS electrolyte. As shown in Fig. 5(b), the response current of GOx/PtAu-rGO/GaN to glucose is remarkable and repeatable ( $36.6 \mu\text{A cm}^{-2}$ ), while its response current to interfering molecules is very small ( $<1.5 \mu\text{A cm}^{-2}$ ) and is about 24-fold lower than that to glucose. It demonstrates that the GOx/PtAu-rGO/GaN sensor has a good selectivity. Long-term stability of GOx/PtAu-rGO/GaN sensor was investigated by measuring the amperometric response to  $1 \text{ mM}$  glucose every 3 days. After 30-day measurement, the current retention of the sensor is  $95.5\%$  [Fig. 5(c)], which indicates that the GOx/PtAu-rGO/GaN

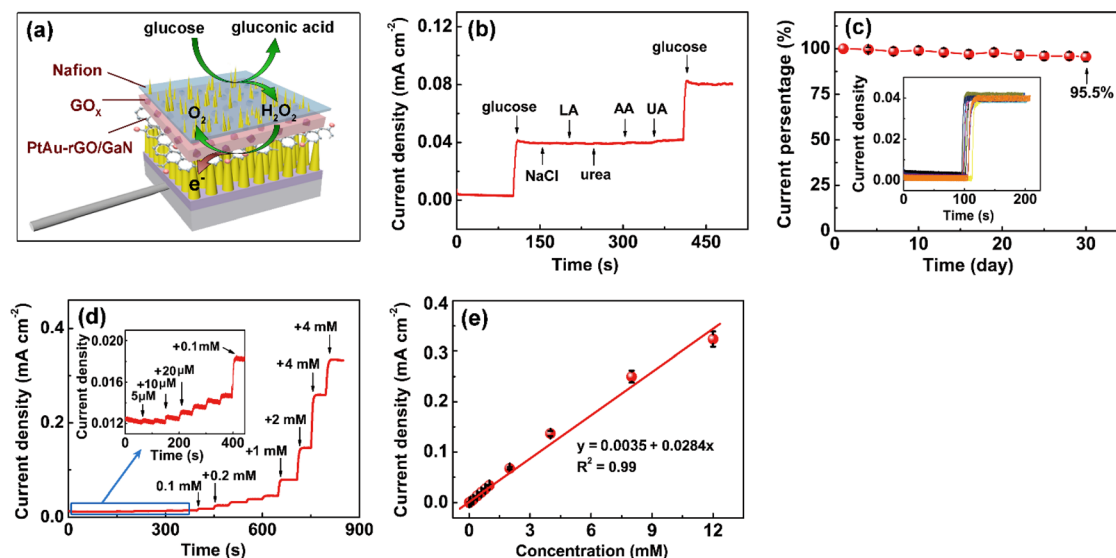


**FIG. 5.** Electrochemical responses of GOx/PtAu-rGO/GaN to glucose in human sweat. (a) Schematic illustration of detection mechanism. (b) Response selectivity to glucose ( $1 \text{ mM}$ ) and interfering molecules ( $0.1 \text{ mM}$ ). (c) Degradation of  $i$ - $t$  response current in  $1 \text{ mM}$  glucose during one-month measurement (inset: amperometric response of GOx/PtAu-rGO/GaN to  $1 \text{ mM}$  glucose). (d) Amperometric response of GOx/PtAu-rGO/GaN with successive addition of glucose at a concentration range of  $0.005$ – $20 \text{ mM}$ . Inset: magnified curve in  $0.005$ – $0.2 \text{ mM}$ . (e) Relationship between response current and glucose concentration.

**TABLE I.** Comparison of the ECSs for glucose detection in sweat. GOx: glucose oxidase; rGO: reduced graphene; SPE: screen-printed electrode; MWCNTs: multi-walled carbon nanotubes; LIG: laser-induced graphene.

Electrodes	Electrolyte	Linear range (mM)	Sensitivity ( $\mu\text{A mM}^{-1} \text{cm}^{-2}$ )	LOD ( $\mu\text{M}$ )	Stability	Reference
GOx/PtAu-rGO/GaN	Human sweat	0.005–12	28.4	5	95.5% (30 d)	This work
GOx-PB/Au	Artificial sweat	0–0.5	13.9	6	...	36
Au-GO/SPE	Artificial sweat	0.00016–5	474.617	123	92% (29 d)	8
GOx-MWCNTs/SPE	Artificial sweat	0–1	105.93	4.95	90.51% (22 d)	6
GOx-Au-PB/Au-Si	Artificial sweat	0.05–1.4	4.7	31	87% (10 d)	9
GOx-PtAu-rGO/Au	PBS	0–2.4	48.5	5	>85% (8 d)	10
GOx-Pt-C/SPE	PBS	0–0.9	105	10	...	11
GOx/Au	PBS	0.025–0.25	0.0021	7	...	12
Cu-Mn/Cu/ppy/cotton	PBS	0–0.4	...	125	...	37
GOx-Pt/LIG/SPE	PBS	0.0003–2.1	65.6	0.3	...	13
Pt/MXene/Pt	PBS	0–8	0.25	29.15	...	38

sensor has a good long-term stability. The reproducibility and repeatability of the GOx/PtAu-rGO/GaN sensor were also investigated (Fig. S14). A relative standard deviation (RSD) in the response current densities is 5.6% and 4.3%, respectively, which indicates that the sensor has a good reproducibility and repeatability.

For detecting glucose in real sweat of human, the amperometric response of the GOx/PtAu-rGO/GaN sensor to human sweat was measured by step increases of glucose solutions to the filtered sweat (0.5 V was chosen as the applied potential, as shown in Fig. S15). As shown in Fig. 5(d), the response current increases linearly with glucose concentration, and a low LOD (i.e., detection accuracy) of  $5 \mu\text{M}$  can be realized. Based on the current-concentration relationship plot [Fig. 5(e)], it can be seen that the linear detection range of the sensor is 0.005–12 mM ( $R^2 = 0.99$ ) with a sensitivity of  $28.4 \mu\text{A} \cdot \text{mM}^{-1} \cdot \text{cm}^{-2}$ , which can cover the glucose concentration in human sweat (0.06–1 mM).<sup>6,7</sup> Moreover, a maximum RSD for the response current is 6.3% during six repeat measurements, indicating the good repeatability of the sensor in sweat.

For comparison, previous reports on ECSs for glucose detection in sweat were summarized in Table I.<sup>6,8–13,36–38</sup> For previously reported ECSs, the linear range and the long-term stability are usually in a range of 0–8 mM and 85%–92%, respectively. In comparison, our GOx/PtAu-rGO/GaN sensor has a wider linear range (0.005–12 mM) and a higher long-term stability (95.5% retention during 30 days). Moreover, the GOx/PtAu-rGO/GaN sensor can be used for detecting glucose in human sweat with good LOD of  $5 \mu\text{M}$ , which is competitive and lower than that of most previously reported ECSs. Thus, GOx/PtAu-rGO/GaN features low LOD, wide linear detection range, and high long-term stability, which is promising for noninvasive glucose detection.

In summary, an ECS based on PtAu-rGO/GaN and GOx/PtAu-rGO/GaN was fabricated and used for glucose detection in PBS electrolyte and sweat, respectively. The GaN NW substrate was employed for ECD of rGO with satisfying dispersion uniformity and anchor strength. The deposited rGO exhibited flake morphology without agglomeration. Moreover, PtAu and rGO can be simultaneously deposited on the GaN NW substrate to realize PtAu-rGO/GaN sensor. In comparison with deposition of PtAu-rGO on the planar SS substrate, PtAu-rGO/GaN demonstrated much higher sensitivity and

long-term stability for glucose detection, owing to better dispersion and anchor strength on GaN NW. With the decoration of GOx, the GOx/PtAu-rGO/GaN sensor can be used for detecting glucose in human sweat with a low LOD of  $5 \mu\text{M}$ , a wide linear detection range of  $5 \mu\text{M}$ –12 mM, and high long-term stability (95.5% retention during 30 days), which demonstrates its potential for noninvasive glucose detection.

See the supplementary material for TEM, SEM, TEM-EDS, GI-XRD analysis, and electrochemical glucose sensing performances of as-prepared sensors.

This research was supported by grants from the New Century Excellent Talents in the University of China (Grant No. NCET-05-0111) and the National Natural Science Foundation of China (Grant No. 62074023).

## AUTHOR DECLARATIONS

### Conflict of Interest

The authors have no conflicts to disclose.

### Author Contributions

**Shunji Chen:** Conceptualization (equal); Data curation (equal); Formal analysis (equal); Investigation (equal); Methodology (equal); Writing – original draft (equal); Writing – review & editing (equal). **Zhefu Chen:** Supervision (equal); Visualization (equal). **Jun Yu:** Supervision (equal); Visualization (equal). **Jianwei Zhang:** Supervision (equal); Visualization (equal). **Hui Huang:** Conceptualization (equal); Funding acquisition (equal); Investigation (equal); Supervision (equal); Writing – review & editing (equal). **Hongqian Xiao:** Investigation (equal). **Yanjie Tang:** Investigation (equal). **Vladimir G. Dubrovskii:** Supervision (equal); Visualization (equal). **Haibin Liu:** Supervision (equal); Visualization (equal). **Peiling Xia:** Supervision (equal); Visualization (equal).

### DATA AVAILABILITY

The data that support the findings of this study are available from the corresponding author upon reasonable request.

## REFERENCES

- <sup>1</sup>F. Xiao, Y. Li, H. Gao, S. Ge, and H. Duan, *Biosens. Bioelectron.* **41**, 417–423 (2013).
- <sup>2</sup>H. Shu, G. Chang, J. Su, L. Cao, Q. Huang, Y. Zhang, and Y. He, *Sens. Actuators B* **220**, 331–339 (2015).
- <sup>3</sup>X. Yang, A. Liu, Y. Zhao, H. Lu, Y. Zhang, W. Wei, and S. Liu, *ACS Appl. Mater. Interfaces* **7**, 23731–23740 (2015).
- <sup>4</sup>G. Chang, Z. Cai, H. Jia, Z. Zhang, X. Liu, Z. Liu, and Y. He, *Int. J. Hydrogen Energy* **43**, 12803–12810 (2018).
- <sup>5</sup>Y. Lin, M. Bariya, H. Y. Y. Nyein, L. Kivimäki, S. Uusitalo, E. Jansson, and A. Javey, *Adv. Funct. Mater.* **29**, 1902521 (2019).
- <sup>6</sup>L. Zheng, Y. Liu, and C. Zhang, *Sens. Actuators B* **343**, 130131 (2021).
- <sup>7</sup>R. Eslami, N. Azizi, S. R. Ghaffarian, M. Mehrvar, and H. Zarrin, *Electrochim. Acta* **404**, 139749 (2022).
- <sup>8</sup>P. Asen, A. Esfandiari, and M. Kazemi, *ACS Appl. Nano Mater.* **5**, 13361–13372 (2022).
- <sup>9</sup>M. Dervisevic, M. Alba, L. Esser, N. Tabassum, B. Prieto-Simon, and N. H. Voelcker, *ACS Appl. Mater. Interfaces* **14**, 2401–2410 (2022).
- <sup>10</sup>X. Xuan, H. S. Yoon, and J. Y. Park, *Biosens. Bioelectron.* **109**, 75–82 (2018).
- <sup>11</sup>A. Abellán-Llobregat, I. Jeerapan, A. Bandodkar, L. Vidal, A. Canals, J. Wang, and E. Morallon, *Biosens. Bioelectron.* **91**, 885–891 (2017).
- <sup>12</sup>M. Yu, Y. T. Li, Y. Hu, L. Tang, F. Yang, W. L. Lv, and G. J. Zhang, *J. Electroanal. Chem.* **882**, 115029 (2021).
- <sup>13</sup>H. Yoon, J. Nah, H. Kim, S. Ko, M. Sharifuzzaman, S. C. Barman, and J. Y. Park, *Sens. Actuators B* **311**, 127866 (2020).
- <sup>14</sup>K. Akbar, S. Hussain, L. Truong, S. B. Roy, J. H. Jeon, S. K. Jerng, and S. H. Chun, *ACS Appl. Mater. Interfaces* **9**, 43674–43680 (2017).
- <sup>15</sup>G. B. Darband, M. Aliofkhaezrai, and S. Shanmugam, *Renewable Sustainable Energy Rev.* **114**, 109300 (2019).
- <sup>16</sup>H. Li, J. Wang, M. Liu, H. Wang, P. Su, J. Wu, and J. Li, *Nano Res.* **7**, 1007–1017 (2014).
- <sup>17</sup>M. Kuang, J. Wang, and L. Jiang, *Chem. Soc. Rev.* **45**, 6833–6854 (2016).
- <sup>18</sup>N. Han, K. R. Yang, Z. Lu, Y. Li, W. Xu, T. Gao, and X. Sun, *Nat. Commun.* **9**, 924 (2018).
- <sup>19</sup>Y. Li, H. Zhang, T. Xu, Z. Lu, X. Wu, P. Wan, and L. Jiang, *Adv. Funct. Mater.* **25**, 1737–1744 (2015).
- <sup>20</sup>H. Li, S. Chen, Y. Zhang, Q. Zhang, X. Jia, Q. Zhang, and X. Wang, *Nat. Commun.* **9**, 2452 (2018).
- <sup>21</sup>S. Chen, H. Huang, H. Sun, Q. Liu, H. Zhu, J. Zhao, and J. Yu, *ACS Appl. Mater. Interfaces* **14**, 49035–49046 (2022).
- <sup>22</sup>S. Zhang, Y. Shao, G. Yin, and Y. Lin, *J. Power Sources* **195**, 1103–1106 (2010).
- <sup>23</sup>K. Bhunia, M. Chandra, S. Khilari, and D. Pradhan, *ACS Appl. Mater. Interfaces* **11**, 478–488 (2019).
- <sup>24</sup>F. Ren, C. Zhai, M. Zhu, C. Wang, H. Wang, D. Bin, and Y. Du, *Electrochim. Acta* **153**, 175–183 (2015).
- <sup>25</sup>P. Wu, H. Liu, Y. Cao, S. Xi, Z. Li, Z. He, and Z. Yan, *Microporous Mesoporous Mater.* **316**, 110982 (2021).
- <sup>26</sup>L. Wang, Y. Dong, Y. Zhang, Z. Zhang, K. Chi, H. Yuan, and S. Wang, *NPG Asia Mater.* **8**, e337 (2016).
- <sup>27</sup>V. H. Pham, T. Gebre, and J. H. Dickerson, *Nanoscale* **7**, 5947–5950 (2015).
- <sup>28</sup>C. Liu, K. Wang, S. Luo, Y. Tang, and L. Chen, *Small* **7**, 1203–1206 (2011).
- <sup>29</sup>X. Yan, X. Ge, and S. Cui, *Nanoscale Res. Lett.* **6**, 1–6 (2011).
- <sup>30</sup>H. Yang, Z. Wang, Q. Zhou, C. Xu, and J. Hou, *Microchim. Acta* **186**, 1–9 (2019).
- <sup>31</sup>F. Gao, F. Zhou, Y. Yao, Y. Zhang, L. Du, D. Geng, and P. Wang, *J. Electroanal. Chem.* **803**, 165–172 (2017).
- <sup>32</sup>K. J. Babu, T. Raj Kumar, D. J. Yoo, S. M. Phang, and G. Gnana Kumar, *ACS Sustainable Chem. Eng.* **6**, 16982–16989 (2018).
- <sup>33</sup>P. Lu, Y. Lei, S. Lu, Q. Wang, and Q. Liu, *Anal. Chim. Acta* **880**, 42–51 (2015).
- <sup>34</sup>M. F. Hossain and J. Y. Park, *PLoS One* **12**, e0173553 (2017).
- <sup>35</sup>J. Ryu, K. Kim, H. S. Kim, H. T. Hahn, and D. Lashmore, *Biosens. Bioelectron.* **26**, 602–607 (2010).
- <sup>36</sup>Y. Zhao, Q. Zhai, D. Dong, T. An, S. Gong, Q. Shi, and W. Cheng, *Anal. Chem.* **91**, 6569–6576 (2019).
- <sup>37</sup>A. Singh, A. Sharma, and S. Arya, *J. Anal. Sci. Technol.* **13**, 11 (2022).
- <sup>38</sup>Q. F. Li, X. Chen, H. Wang, M. Liu, and H. L. Peng, *ACS Appl. Mater. Interfaces* **15**, 13290–13298 (2023).